AGU100 ADVANCING EARTH AND SPACE SCIENCE

JGR Solid Earth

RESEARCH ARTICLE
10.1029/2019JB018364

# The Effect of Brine on the Electrical Properties of Methane Hydrate

R. Lu[1], L. A. Stern[2], W. L. Du Frane[1], J. C. Pinkston[2], J. J. Roberts[1], and S. Constable[3]

[1]Lawrence Livermore National Laboratory, Livermore, CA, USA, [2]U.S. Geological Survey, Menlo Park, CA, USA, [3]Scripps Institution of Oceanography, La Jolla, CA, USA

**Key Points:**

- Electrical properties of a multicomponent methane hydrate system synthesized from a mixture of ice, NaCl, and $CH_4$ gas were examined
- Electrical conductivity of samples increases nonlinearly with increasing salt content for temperatures above −15 °C
- No secondary NaCl-bearing phases were detected in samples with <1.0 wt % salt due to possible incorporation into the hydrate structure

**Supporting Information:**

- Supporting Information S1

**Correspondence to:**
L. A. Stern and W. L. Du Frane,
dufrane2@llnl.gov;
lstern@usgs.gov

**Citation:**
Lu, R., Stern, L. A., Du Frane, W. L., Pinkston, J. C., Roberts, J. J., & Constable, S. (2019). The effect of brine on the electrical properties of methane hydrate. *Journal of Geophysical Research: Solid Earth*, *124*, 10,877–10,892. https://doi.org/10.1029/2019JB018364

Received 11 JUL 2019
Accepted 25 SEP 2019
Accepted article online 16 OCT 2019
Published online 6 NOV 2019

**Abstract** Gas hydrates possess lower electrical conductivity (inverse of resistivity) than either seawater or ice, but higher than clastic silts and sands, such that electromagnetic methods can be employed to help identify their natural formation in marine and permafrost environments. Controlled laboratory studies offer a means to isolate and quantify the effects of changing individual components within gas-hydrate-bearing systems, in turn yielding insight into the behavior of natural systems. Here we investigate the electrical properties of polycrystalline methane hydrate with ≥25% gas-filled porosity and in mixture with brine. Initially, pure methane hydrate was synthesized from $H_2O$ ice and $CH_4$ gas while undergoing electrical impedance measurement, then partially dissociated to assess the effects of pure pore water accumulation on electrical conductivity. Methane hydrate + brine mixtures were then formed by either adding NaCl (0.25–2.5 wt %) to high-purity ice or by using frozen seawater as a reactant. Conductivity was obtained from impedance measurements made in situ throughout synthesis while temperature cycled between +15 °C and −25 °C. Several possible conduction mechanisms were subsequently determined using equivalent circuit modeling. Samples with low NaCl concentration show a doping/impurity effect and a log linear conductivity response as a function of temperature. For higher salt content samples, conductivity increases exponentially with temperature and the log linear relationship no longer holds; instead, we observe phase changes within the samples that follow NaCl–$H_2O$–$CH_4$ phase equilibrium predictions. Final samples were quenched in liquid nitrogen and imaged by cryogenic scanning electron microscopy (cryo-SEM) to assess grain-scale characteristics.

## 1. Introduction

Gas hydrates, also called clathrate hydrates, are ice-like substances with encaged gas molecules (Sloan, 1998). Most naturally occurring gas hydrate contains methane and typically forms under conditions with abundant free or dissolved gas, elevated pressures, and cool temperatures, as may occur in certain marine and permafrost regions worldwide (Kvenvolden, 2000; Maslin et al., 2010). Nearly 99% of the world's methane hydrate forms in sediments of deep marine continental margins, typically at water depths greater than 300–500 m (Kvenvolden, 2000; Mclver, 1981; Ruppel, 2015). Methane hydrate can also form in shallower deposits or even directly on the seafloor where methane seeps into the ocean (Ruppel & Kessler, 2017). There is keen interest in methane hydrate as a potential energy source as well as its role in the global carbon cycle and for geohazard concerns (Archer, 2007; Boswell & Collett, 2011; Ruppel & Kessler, 2017). Many deposits have already been characterized, but there are still uncertainties in the exact volume of these reservoirs (Collett et al., 2015).

Seismic imaging and well logging are current geophysical methods for identifying gas hydrate deposit locations around the world (Liang et al., 2017; Trehu et al., 2004). Seismic imaging can be facilitated by the existence of a bottom-simulating reflector (BSR) along the edge of the methane hydrate and free gas phase boundary in marine sediments (Hornbach et al., 2003). However, there are cases where BSRs do not coincide with gas hydrate layers, with some layers situated well above or below the BSRs (Majumdar et al., 2016; Shedd et al., 2012). Furthermore, seismic imaging of BSRs reveals little about gas hydrate concentration and there are cases where gas hydrates with lower saturations are known to exist, but exhibit no BSR signature due to a lack of sharp discontinuity in the seismic velocity profile (Chong et al., 2016; Sloan & Koh, 2007; Weitemeyer et al., 2011; Wood et al., 2002). Well logging or coring provides a more accurate assessment of saturation with depth, but is expensive and provides only a single location inferring the presence of gas hydrates (Lee & Collett, 2011).

An alternative geophysical method involving electromagnetic (EM) remote sensing techniques can provide a complementary solution to seismic imaging for determining concentration and geometric distribution of gas hydrates in subseafloor structures (Attias et al., 2016; Weitemeyer et al., 2006). Controlled-source electromagnetic (CSEM) surveying methods are sensitive enough to detect the higher resistivity of gas hydrate relative to pore fluids in sediments (Constable et al., 2016). The resistivities measured from CSEM methods can be converted to hydrate saturation via Archie's equation and 3-D inversion for conductivity models (Archie, 1942; Attias et al., 2018). However, the derived hydrate saturation values may not be accurate due to uncertainty in the estimation of the parameters of Archie's equation (Cook & Waite, 2018). Developing a more fundamental understanding of the petrophysical relations between methane hydrate and brine salinity should therefore help to better correlate resistivity data with methane hydrate saturations, and in turn improve reliability of existing and new models. Well log measurements also utilize resistivity for detection of gas hydrate and may benefit from the results of this study.

Although physical properties of methane hydrate have been studied extensively via lab-synthesized samples (Sloan & Koh, 2007, and references therein), there are only a limited number of investigations of their electrical properties: gas hydrate in pore spaces of glass beads (Spangenberg & Kulenkampff, 2006); gas hydrate with quartz sand (Du Frane et al., 2015; Ren et al., 2010); gas hydrate with sand, silt, and clay (Lee et al., 2010); and pure polycrystalline methane hydrate (Du Frane et al., 2011). When resistivity relations are applied to Archie's and other mixing law models, one can determine hydrate saturation levels based on electrical characteristics (Cai et al., 2017). These previous studies are useful for simulating conditions of natural gas hydrates or creating simplified systems for modeling purposes.

The presence of brine in porous media has been shown to affect both gas hydrate formation (You et al., 2015) and its electrical conductivity (Li et al., 2012). Li et al. (2012) demonstrated that salinity, temperature, and hydrate saturation level can potentially influence the electrical response by several orders of magnitude. Although their results provide important insights and trends, they used a single alternating current frequency which does not fully isolate the specific sample response from contributions of the electrode polarization. Hence, additional information can be gleaned from further investigation using impedance spectroscopy over a broad range of frequencies. For example, impedance spectroscopy can help reveal variations in electrical behavior, conduction mechanisms/pathways, composition distributions, and other internal changes in a material system just by varying current frequencies (Roberts, 2002; Roberts & Tyburczy, 1999). Gas hydrate/sediment mixtures are dielectrics with electrical behavior that is strongly dependent on temperature (Du Frane et al., 2015), and obtaining quantitative information on the subtleties that contribute to the overall electrical response of gas hydrate mixtures is crucial for understanding more complex systems.

To date, there is little-to-no published work investigating the electrical properties of pure methane hydrate in contact with seawater salts/NaCl and in the absence of sediments. Our motivation here is twofold: (1) to isolate and quantify the effects on electrical properties of methane hydrate when adding known quantities of salts to the bulk system in a controlled manner and (2) to better understand the influence of salts as both a potential impurity (or doping agent) within the hydrate grains themselves and in the development of intergranular pore fluid (brine). Toward these ends, we first synthesized pure methane hydrate (0 wt % NaCl) and measured electrical conductivity to ensure consistency with previous (Du Frane et al., 2011, 2015) results. We then measured the same sample after inducing partial dissociation at +5 °C via depressurization, to monitor conductivity changes caused by generating pure $H_2O$ pore liquid within the specimen. We next measured electrical conductivity of methane hydrate with total NaCl bulk concentrations ranging from 0.25 to 2.5 wt %, by synthesizing samples from three-component mixtures of pure ice + salt + methane gas in a manner allowing uniform distribution of NaCl throughout the sample. Lastly, we synthesized and measured methane hydrate prepared from frozen synthetic seawater (3.5 wt % salts) + methane gas. Impedance spectroscopy with frequencies between 0.5 and 300 kHz were measured and analyzed for all samples between +15 °C and −25 °C. The results allowed correlation of pore fluid fractions with bulk sample conductivity, which in turn can be approximated using petrophysical mixing models. Gas hydrates occur in nature both above and below 0 °C, and investigating both the high- and low-temperature regimes allows us to better assess the physical and chemical constituents and changes that occur in each sample as a function of temperature. Hydrate grain-scale characteristics including grain size, intergranular porosity, grain morphology, contacts, and distribution of phases were also evaluated on final, quenched samples by cryogenic scanning electron microscopy.

## 2. Materials and Methods

### 2.1. Sample Preparation

For sample preparation, triple-distilled water frozen to gas-free ice chunks were crushed and sieved to 180–250 μm to form granular "seed ice" (method described by Stern et al., 1996, 2004). One sample was prepared from pure $H_2O$ seed ice (sample NH0, with no added NaCl), whereas most were prepared from seed ice mixed with salt. For salt-added samples, sodium chloride (NaCl) crystals >99.9% purity (VWR International) were powdered by mortar and pestle, then sieved to <75 μm. The goal was to uniformly distribute the smaller salt crystals throughout the ice by positioning them along ice grain boundaries and in ice grain junctions, such that they would dissolve during sample synthesis to form a well-distributed brine network around methane hydrate grains or clusters of grains. The powdered NaCl was initially cooled below −50 °C to prevent any premature reaction with the ice, then thoroughly mixed with the granular ice using a spatula in a conventional −25 °C freezer. Samples were prepared with varying proportions of ice and NaCl as listed in Table 1. One additional sample was prepared using seed ice made from synthetic seawater in place of triple-distilled water. Synthetic seawater was purchased from High-Purity Standards, Inc. (ISO certified) with 3.5 wt % as total salts and 2.7 wt % as NaCl. The seawater was flash-frozen as droplets in liquid nitrogen to maintain uniform salinity both within and amongst all grains, then crushed and sieved to <250 μm.

The granular ice + salt reactants were then poured into insulating FEP plastic tubing (50.8-mm diameter × ~90 mm tall), compacted to 10-mm thickness, sandwiched between two same-diameter silver electrodes, sealed in a custom high-pressure vessel, and attached to the synthesis apparatus such that the cell was fully immersed in a −25 °C d-Limonene fluid bath (Du Frane et al., 2011, Figure 1). Initial porosity for all samples was ~36 vol % (Table S1 in the supporting information). Samples were then ready to be synthesized while simultaneously collecting in situ impedance (Z) spectroscopy measurements.

To begin synthesis, sample pore space was briefly evacuated and then flooded with chilled, high-pressure methane ($CH_4$) gas at ~20 MPa and −25°C, placing the reactants deep within the methane hydrate stability field. Temperature of the surrounding fluid bath was then heated to +15 °C at ~11 °C/hr and held for ~15 hr for the first cycle (then 12-hr holds for subsequent cycles) with isochoric $CH_4$ pressures increasing to ~28 MPa. During this time most of the ice grains react along their surfaces to form methane hydrate as they pass through the ice point, as demonstrated in Stern et al. (1996, 2004). To ensure full reaction, including dissolution of the NaCl, samples were subjected to repeated temperature cycling between +15 °C and approximately −25 °C (total 30–35 hr per cycle). During the high-temperature portions of synthesis, the ice, salt, and methane mixtures react to form a multicomponent system where the resulting methane hydrate coexists with an NaCl-bearing fluid phase ("brine"). Upon cooling below 0 °C and down to −24 °C, the composition of the brine evolves with time and temperature as first ice and then hydrohalite ($NaCl·2H_2O$) begin crystallizing in accordance with NaCl-$H_2O$ phase equilibria (Figure 1; see also McCarthy et al., 2007, Figure 3). Hence, during each thermal cycle, samples pass through multiple phase boundaries in the $CH_4$-$H_2O$-NaCl phase diagram (Figure 1, shaded green region).

Each sample underwent a minimum of six thermal cycles and until electrical impedance stopped changing significantly between cycles (<5% impedance change on log-scale), to ensure that the sample had stabilized and that methane hydrate synthesis in the mixed-phase system was complete. A final incremental heating step, referred to here as "step-dwell," involved a 1-hr hold at each target temperature to allow thermal equilibration of the sample before performing an impedance frequency sweep to calculate electrical conductivity. Each full run lasted approximately 300–400 hr. Electrical conductivity of samples at temperatures below −20 °C was obtained during the normal cooling cycle of the freezer, which slows to a rate below 1 °C/hr as it approaches a minimum temperature.

To obtain methane hydrate with in situ pore water rather than brine, we briefly destabilized the fully synthesized pure methane hydrate sample (Sample NH0) by depressurizing across the phase stability boundary while holding external temperature at +5 °C and allowing the sample to partially dissociate to water + gas (Figure 2a). This method was chosen to destabilize the disk-shaped sample as homogeneously as possible and to promote uniform accumulation of dissociated water, by minimizing heat flow gradient effects that accompany dissociation by external thermal ramping. Pressure was slowly released from 20 to 5 MPa,

**Table 1**
*Sample Conditions of Methane Hydrate Initially Prepared with Added NaCl (NH-series) and from Seawater (SH) During Synthesis*

| | Starting seed ice (wt %) | Starting salt concentration (wt %) | No. of synthesis cycles | Step-dwell overall heating rate (°C/hr) | $CH_4$ pressure range (MPa) | Temperature range (°C) |
|---|---|---|---|---|---|---|
| NH0[a] | 100 | 0 | 6 | 2.7 | 18.1–23.5 | −18 to +15 |
| NH0.25 | 99.75 | 0.25 | 9 | 1.3 | 19.1–26.6 | −25 to +15 |
| NH1.0 | 99.0 | 1.0 | 8 | 2.9 | 18.9–25.4 | −25 to +15 |
| NH1.75 | 98.25 | 1.75 | 10 | 2.5 | 19.0–26.7 | −25 to +15 |
| NH2.5 | 97.5 | 2.5 | 11 | 2.5 | 19.7–28.0 | −25 to +15 |
| SH3.5[b] | 96.5 | 3.5 | 9 | 0.9 | 21.5–29.8 | −23 to +15 |

[a] NH0 is pure methane hydrate but underwent partial dissociation after the step-dwell measurement. [b] SH3.5 (Methane hydrate synthesized from frozen seawater) was prepared differently than samples NH0-NH2.5 as described in experimental methodology.

allowing sufficient time for sample equilibration following isochoric cooling effects. Pressure was then reduced again to ~3.8 MPa, ~0.6 MPa below the equilibrium boundary, to induce partial dissociation and in situ production of pore water. After pressure rebounded from the dissociation process and impedance approached a new plateau, the NH0 sample was quenched in liquid nitrogen for cryo-SEM analysis of pore water distribution within the sample (Figure 2b).

Porosity of final, as-synthesized samples ranged from approximately 25 to 27 vol %, with increasing porosity trending with increasing NaCl content. Sample NH0 (pure methane hydrate), prior to dissociation, contained ~25 vol % of methane gas-filled intergranular porosity, as calculated from the measured mass of the reactant ice and the expected volumetric increase (~17% from Kuustraa & Hammershaimb, 1983) upon its restructuring to a structure I clathrate hydrate lattice (see Table S2 for porosity calculations). All NaCl-bearing samples contained higher porosities, ranging upward of 27 vol %, caused by additional volume changes associated with a portion of the reactant ice melting to dissolve the added NaCl rather than expanding to form hydrate, plus the eliminated volume of the powdered NaCl(s) itself during dissolution (Table S2). Run SH3.5 is expected to continue this trend and contain even higher porosity, but is not quantified here. We note that the calculated porosities are the minimum possible and assume full NaCl-saturation of the brine. Porosity may be higher if the brine is not fully saturated throughout the sample.

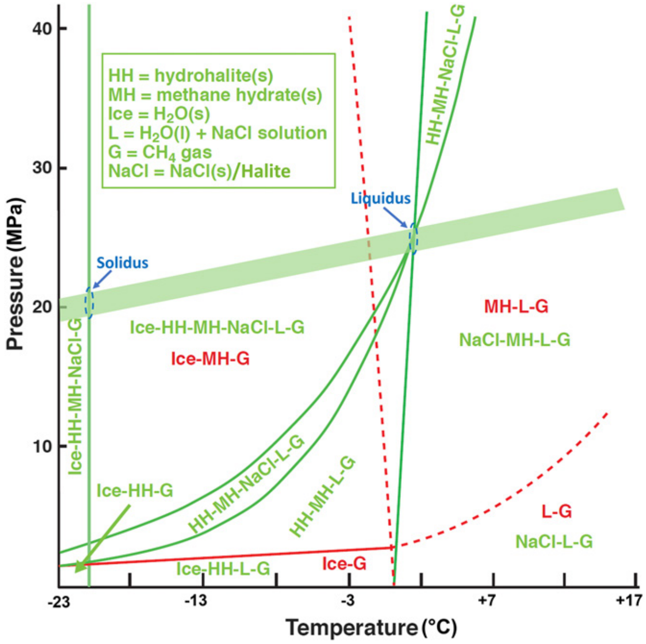

**Figure 1.** Phase diagram of the ternary system $CH_4$-$H_2O$-NaCl (green lines) modified from De Roo et al. (1983). Experimental isochoric pressure-temperature conditions for all samples during heating/cooling cycles fall within the shaded green region. The solidus and liquidus of the sample mixture systems are marked as blue dotted ovals. The red lines and text indicate the binary system $CH_4$-$H_2O$ without NaCl, although the presence of NaCl can alter the location of the phase stability boundary (e.g., Cha et al., 2016). For NaCl-$H_2O$ binary system, see Figure 3 in McCarthy et al. (2007).

## 2.2. Electrical Characterization

Impedance spectroscopy measurements (0.5–300 kHz) were collected on a GwINSTEK LCR 6300 (Inductance, Capacitance, and Resistance) meter for each run. The instrument and experimental setup were tested for electrical leakage using a Teflon blank and various parallel resistor-capacitor (RC) circuits. This was done to verify no significant electrical leakage occurred during runs with methane hydrate samples. At an interface, physical properties (such as compositional or crystallographic) may change precipitously and cause heterogeneous charge distributions (polarizations) that reduce the overall electrical conductivity of a system (Barsoukov & Macdonald, 2005). Collecting impedance spectra over a large range of frequencies was necessary to isolate the electrical conductivity of the bulk samples from systemic contributions such as polarization from the electrode-sample interface which is common in dielectric materials, e.g. gas hydrates (Roberts & Tyburczy, 1994, 1999).

Previous conductivity studies (Du Frane et al., 2011, 2015) on methane hydrate demonstrated that the impedance used to calculate electrical conductivity can be reliably measured at the frequency associated with the smallest phase angle (phase shift between the input voltage and measured current) since pure methane hydrate exhibits capacitive behavior due to its

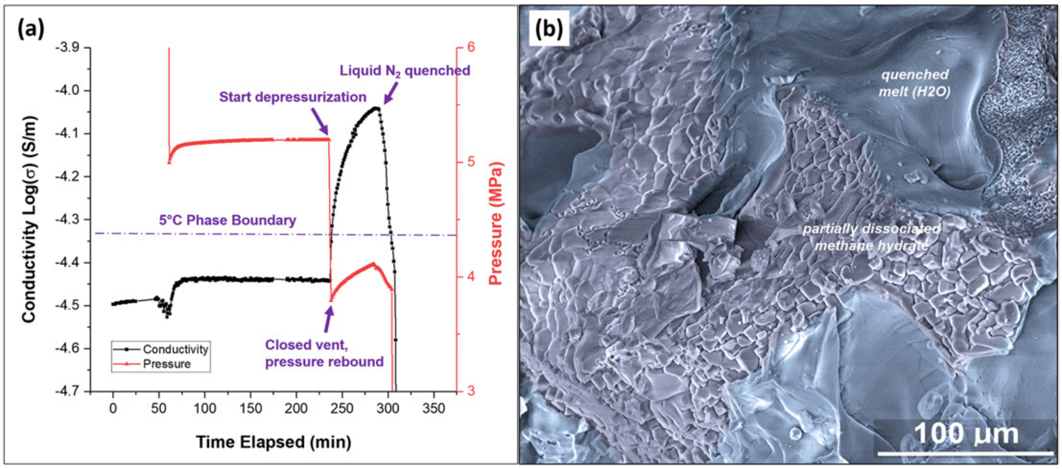

**Figure 2.** (a) Conductivity response when partially dissociating pure methane hydrate (Sample NH0) by decreasing pressure at +5 °C (278 K) to induce pore water formation. Conductivity was calculated as the inverse of the impedance resistance response at 70 kHz. (b) Cryo-SEM image showing regions of accumulated pore water in partially dissociated methane hydrate. The water, quenched here to ice (digitally highlighted in blue), tends to amass into small pools but is uniformly distributed throughout the sample (see also Figure S3 in the supporting information).

dielectric nature. However, when introducing NaCl into the system, the samples may possess either dielectric or conductor-like properties depending on the temperature and the phases (liquid/solid) present. Hence, more rigorous equivalent circuit modeling (ECM) is required to fit the impedance spectroscopy measurements. Using the resistance (R) values from the ECM fits proved more reliable for the calculation of the electrical conductivity instead of identifying one specific frequency (at the smallest phase angle)

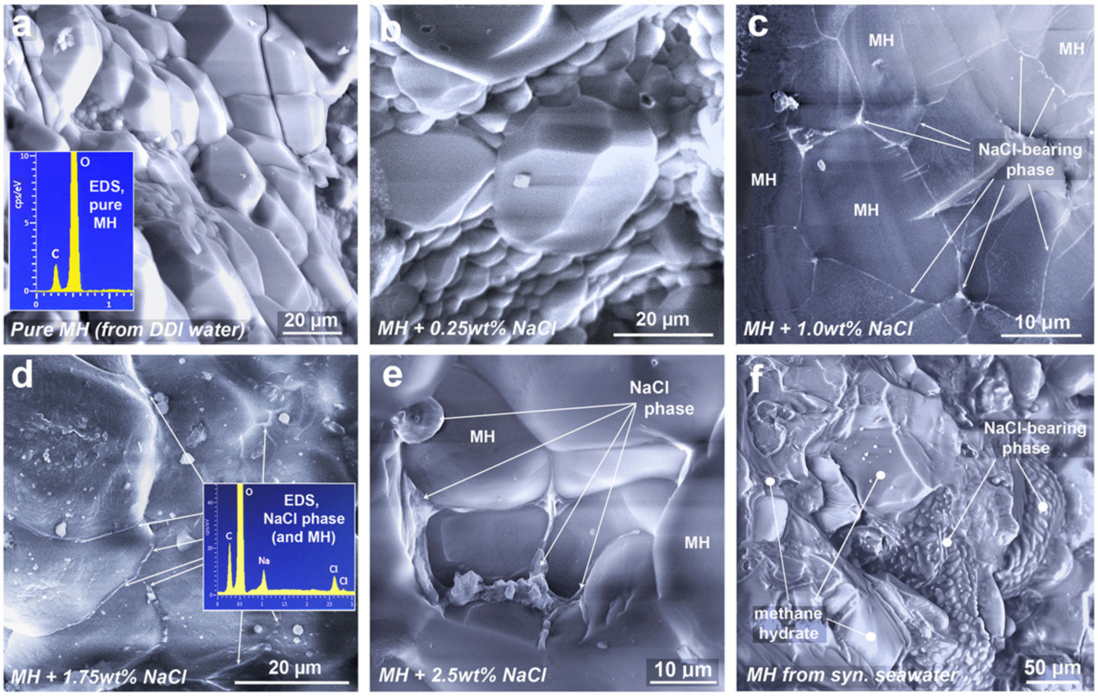

**Figure 3.** Cryo-SEM images of quenched methane hydrate (MH) samples formed by methods described in the text. (a) Pure methane hydrate with EDS spectra showing the expected carbon and oxygen peaks, (b) Sample NH0.25, (c) Sample NH1.0, (d) Sample NH1.75 with EDS spectra demonstrating the expected Na and Cl peaks of the frozen NaCl-bearing phase, (e) Sample NH2.5, and (f) Sample SH3.5. Methane hydrate is the dominant phase in all images and typically appears here as the darker/smoother material. Examples of the NaCl-bearing crystalline or frozen brine phase, confirmed by EDS, are pointed out in (c)–(f) and typically develop into a partially or fully interconnected network between methane hydrate grains during sample synthesis. Additional images are in Figure S2.

associated with an impedance value. ECM fitting was performed on EIS Spectrum Analyzer software (Bondarenko & Ragoisha, 2005). Conditions for fits are based on 3,000 iterations using the Powell algorithm and an unweighted (complex nonlinear least squares) function.

Following synthesis and final impedance measurement, samples were recovered for analysis of phase distribution and grain-scale characteristics using a scanning electron microscope equipped with a cryogenic stage (cryo-SEM) similar to that described by Stern et al. (2004). The pressure vessel containing the sample was first quenched with liquid nitrogen while methane gas pressure was slowly released, and the methane hydrate sample was then extracted, measured, and stored in liquid nitrogen prior to SEM analysis. The cryo-SEM setup involves a specialty preparation chamber and imaging stage (Gatan Alto1000) attached directly to a Tescan variable-pressure SEM (Figure 1b in Lu et al. (2018)). Small sections of samples were first cleaved under vacuum in the cryo-preparation chamber to obtain fresh surfaces uncontaminated by water condensation, then transferred directly to the imaging stage. Imaging was conducted at <−185 °C, 10–15 kV, under low-vacuum mode of ~20 Pa.

## 3. Results

### 3.1. Cryogenic Scanning Electron Microscopy

Cryo-SEM examination of sample NH0 (methane hydrate sample that was partially dissociated; Figure 3a) and sample NH0.25 (with the lowest added NaCl content in the study; Figure 3b) shows uniform development of polycrystalline methane hydrate grains typically ranging between 5 and 80 μm, and sometimes larger (>100 μm) where they border open pores. Energy dispersive X-ray spectroscopy (EDS) spot measurements on methane hydrate clearly show the carbon elemental peak in addition to the oxygen peak (Figure 3a, inset), differentiating methane hydrate from ice. Neither the elemental Na or Cl signals were present in EDS spectra of sample NH0.25, or were simply below the limit of detection. For higher salt content samples, the observed frozen brine (primarily compositions of microcrystalline ice + hydrohalite ± halite) becomes evident as thin rims surrounding methane hydrate grains and develops into increasingly interconnected networks with increasing salt content (Figures 3c–3e). This is in agreement with the tendency of gas hydrates to exclude impurities during crystal formation (Hesse & Harrison, 1981). However, crystal habit development of the methane hydrate grains visually deteriorates with increasing NaCl content, with higher NaCl-bearing samples exhibiting significantly poorer development of well-defined isometric structures (compare Figures 3a and 3b to 3d and 3e; see also Figure S1). In any case, the NaCl-bearing phase can be visually and chemically differentiated from the methane hydrate grains by both SEM and EDS (compare Figure 3a inset with 3d inset). Additional cryo-SEM images showing the NaCl-bearing phase distribution in samples are provided in Figure S2.

Sample SH3.5 formed from flash-frozen seawater (Figure 3f) exhibits considerably different grain-scale characteristics compared to samples formed from ice grains premixed with salt. Here there are few areas that show thin or distinct borders of frozen brine around pure methane hydrate; instead, broader regions or sometimes branching or dendritic formations of NaCl-bearing frozen material formed throughout the sample, confirmed by EDS. In other regions bordering on open cavities, the frozen NaCl phase developed a botryoidal appearance (Figure 3f). Methane hydrate grains in the seawater sample were also found to be significantly more rounded compared to those from samples with no or low salt content (Figure S1).

Cryo-SEM imaging of pure methane hydrate after partial dissociation (NH0) revealed development of the liquid water by-product, quenched in place prior to imaging, forming loosely interconnected accumulations distributed throughout the sample (Figure 2b; see also Figure S3). On the basis of numerous images, we estimate that the sample contained approximately 15 ± 5 vol % dissociated water when the test was terminated and sample quenched (Figure 2a). Methane hydrate grains in this example show a general reduction in grain size compared with undissociated samples (compare Figures 2b and 3a), with grains exhibiting rounding or receding of crystal facets as they destabilize to form pore liquid.

### 3.2. Impedance Spectroscopy

During hydrate synthesis, sample NH0 and NH0.25 show impedance responses that are frequency dependent (Figures S4a and 4a, respectively) throughout the full temperature range. For samples with higher NaCl content (NH1.0 or NH1.75), there is a much larger impedance spread for different frequencies at the lower temperature regions (<0 °C), typical of a dielectric-like material. In contrast, at higher temperatures

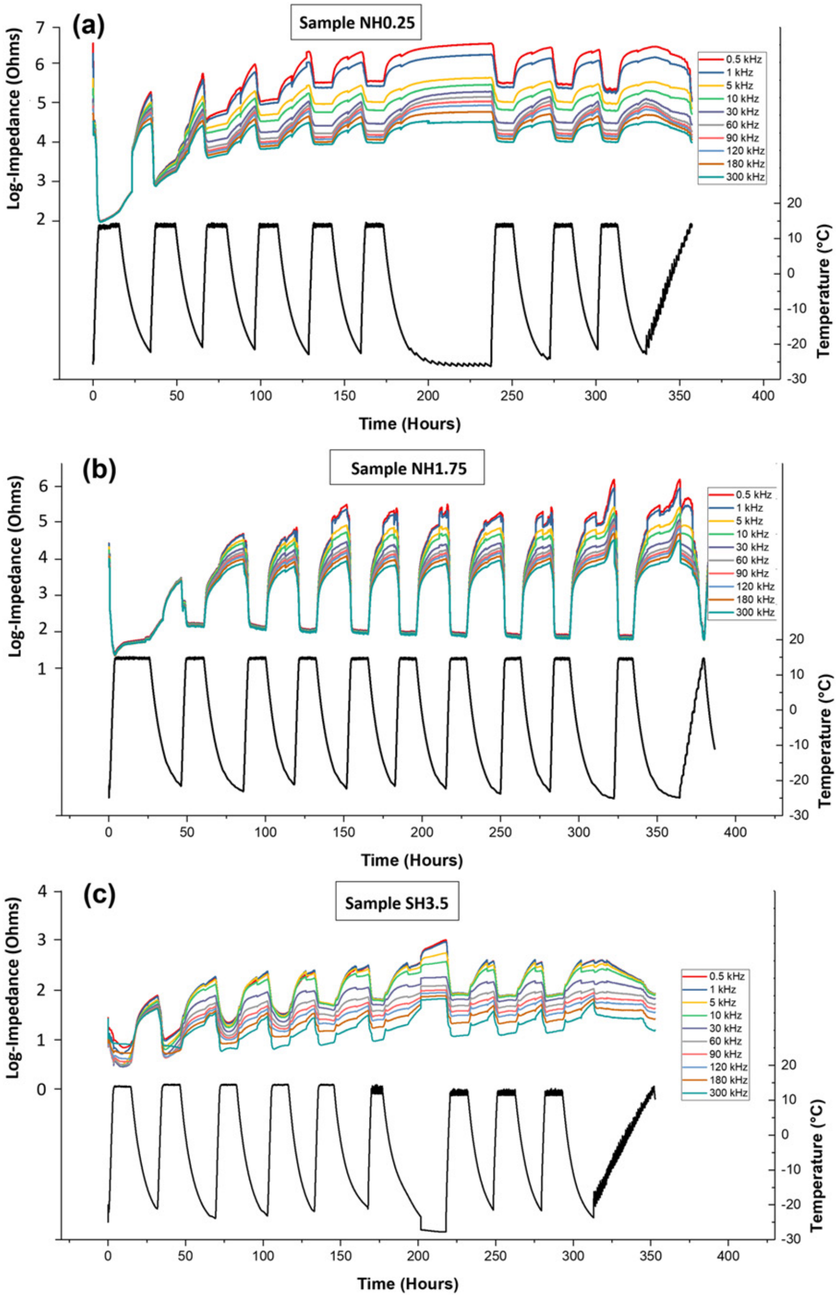

**Figure 4.** Impedance at various frequencies measured during synthesis temperature cycling for several samples. (a) NH0.25, (b) NH1.75, and (c) SH3.5. A slow step-dwell heating cycle is included at the end of each plot; see text for further description. See Figure S4 for similar plots of samples NH0, NH1.0, and NH2.5.

for samples NH1.0/1.75, the spread in impedance response is narrower with much less frequency dependence, typical of a conductor-like material (Figures S4b and 4b). However, this impedance frequency spread-temperature relationship no longer holds true for methane hydrate samples (NH2.5 and SH3.5) with the highest salt contents (Figures S4c and 4c). Both samples appear to exhibit electrical behaviors similar to a conductor-like medium for all temperatures above >−24 °C.

In order to further examine the electrical contributions from different specific frequencies, complex Z-spectra (Cole-Cole plots) that compare imaginary impedance versus real impedance are plotted for each methane hydrate sample (Figure 5). The higher-frequency region (>10 kHz) is typically attributed to electrical

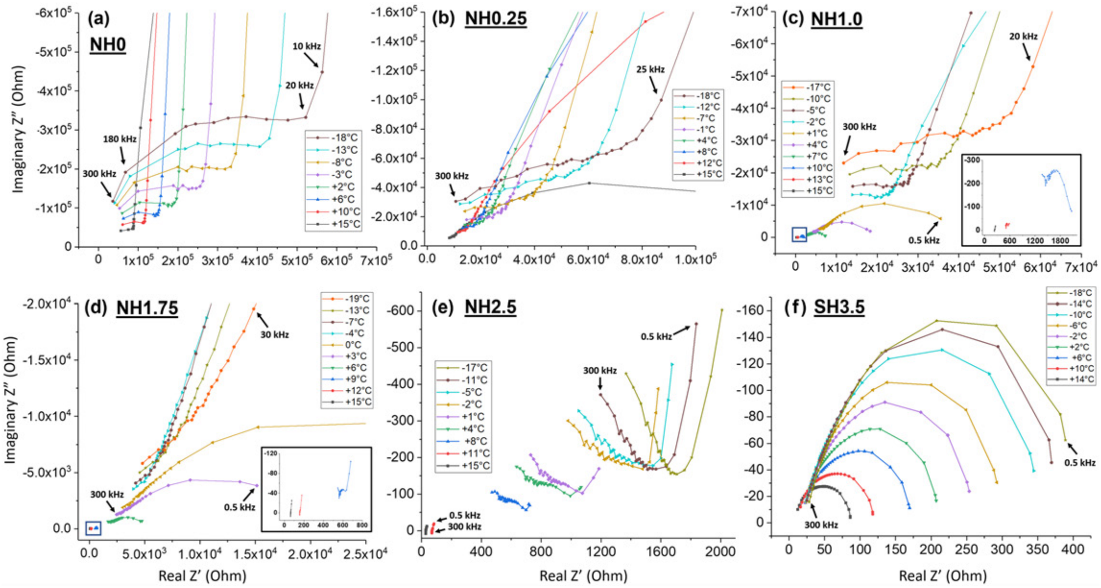

**Figure 5.** Complex Z-spectra comparing imaginary impedance versus real impedance for variable frequencies (0.5–300 kHz) of all samples as a function of temperature. Each point in each temperature plot represents a specific frequency. (Highest frequency on the left side of the *x* axis and lowest frequency on the right side.) Samples (a) NH0, (b) NH0.25, (c) NH1.0, (d) NH1.75, (e) NH2.5, and (f) SH3.5 are plotted. Some plots (a–d) are cropped to show high-frequency (>10 kHz) regions associated with bulk sample conductivity. Plots (e) and (f) show the full frequency range measured.

properties of the bulk hydrate sample while the lower frequencies (<10 kHz) are likely associated with electrode polarization (double-layer capacitance) at the hydrate sample-electrode interface, which is common for a dielectric material (methane hydrate) in contact with a conductor such as a silver foil electrode (Du Frane et al., 2011). This is because low electrical frequencies (<10 kHz) can be obstructed by the electrode polarization resulting in electrical resistance values significantly higher than that of the bulk hydrate sample alone. Methane hydrate samples with added salt exhibit more dramatic changes in their spectra curves with relative changes in temperature, which can be attributed to differences in dielectric relaxation times (Das & Bhattacharyya, 2011). The time-dependent responses in phase and amplitude changes can reveal how electrons interact with the electrode-sample surface. At higher temperatures, the impedance contribution from electrode polarization diminishes (smaller imaginary and real ohmic resistance) and this is especially true for methane hydrate samples with high salt contents (Figures 5c–5f).

### 3.3. Equivalent Circuit Modeling

To understand how the conductive pathway is changing as a function of salt content and temperature, equivalent circuit models (ECM) for methane hydrate samples at various temperatures and salt contents were obtained (Figure 6). These ECMs are the simplest models required to adequately fit each complex Z-spectra (Figure 5) with less than 5% error in the fitted resistance (R) values for the high frequency region (>10 kHz), representative of the bulk sample. The ECMs verify that different conduction mechanisms exist for methane hydrate at different salt contents and temperatures. For pure methane hydrate (sample NH0) at relatively cool temperatures, two resistor-capacitor circuits in series reflect two interfaces that electrons must pass through, denoted "RC+RC" (Figure 6a). One RC circuit represents the bulk hydrate sample and the other corresponds to the electrode-sample interface. This ECM is consistent with the model for pure methane hydrate samples from previous reports (Du Frane et al., 2011). However, at higher temperatures (Figure 6b), ECM fitting required replacing one of the capacitors with a constant phase element (CPE) due to the low-frequency second arc in the Z-complex spectra becoming less than 90°. This circuit model is denoted "RCPE+RC." The CPE in a circuit typically indicates a system experienced microstructural and/or morphology changes that caused nonuniformities in the current distribution (Rodriquez Presa et al., 2001; Shoar Abouzari et al., 2009). Due to these physical/compositional changes, the use of simple ideal resistor and capacitor elements is no longer adequate in the fits for modeling these systems. We see that with increasingly higher temperatures and salt contents, both capacitors in the ECMs become CPEs, denoted "RCPE

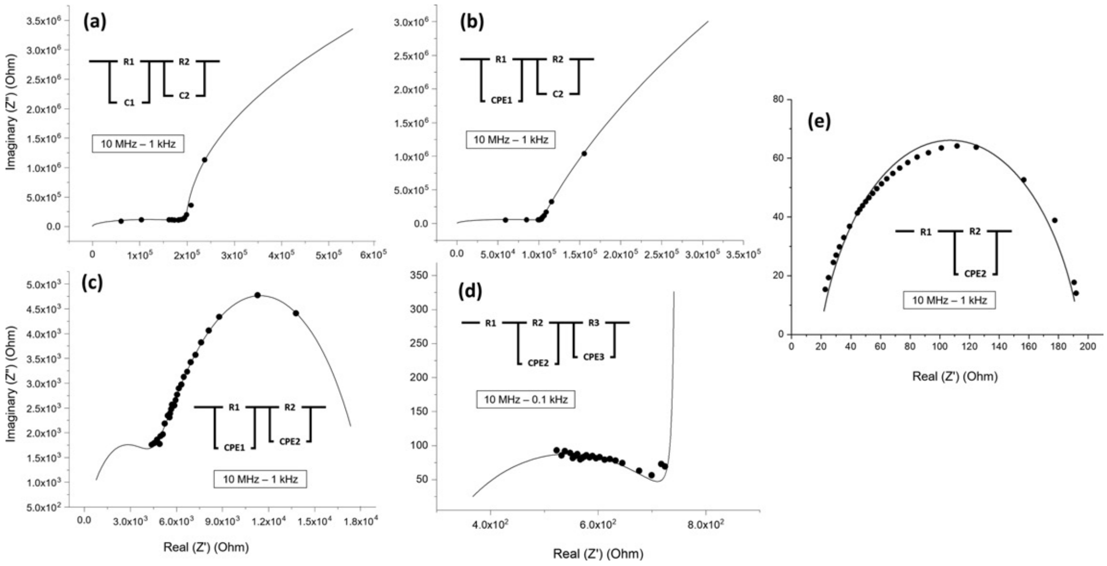

**Figure 6.** Equivalent circuit models for various NaCl content and temperatures. Example of simulated fits for the five possible equivalent circuit models. Models for sample (a) NH0 at +3 °C, (b) NH0 at +15 °C, (c) NH1.0 at +4 °C, (d) NH2.5 at +8 °C, and (e) SH3.5 at +4 °C. These are the simplest equivalent circuit models required to obtain acceptable fits with <5% error in the fitted resistance (R) values. The frequency range modeled is illustrated as thin line plots. Actual experimental data are the circular dot plots.

+RCPE" (Figure 6c). Eventually, at sufficiently high temperatures and salt contents (Figure 6d), a new resistor element was added in series into the ECMs to achieve a better fit, denoted "R+RCPE+RCPE." For the seawater-hydrate sample (Figure 6e), a small amount of electrode polarization can be resolved for our measured frequency range at the electrode-sample interface and only resistance but no capacitance is observed in the bulk hydrate sample itself. The ECM for this system is simply "R+RCPE."

### 3.4. Electrical Conductivity

Knowing the complex Z-spectra and obtaining R-values from the ECM fits, the sample conductivity (inverse of resistivity) for each salt and temperature condition was calculated. In general, there is a clear trend in which higher temperature and salt content in the hydrate samples correspond to higher electrical conductivity (Figure 7). To better understand these results, different geometric markers are used to depict the five possible ECMs. For samples NH1.0, NH1.75, and NH2.5 at sufficiently high temperatures, the conduction mechanisms can be modeled with the R+RCPE+RCPE circuit whereas the others lack this third resistor component. The seawater-hydrate sample exhibited the highest conductivity, as expected, due to having the highest salt content. Conductivity of the partially dissociated (PD) pure methane hydrate is also plotted to compare the effects of pure $H_2O$ pore water versus brine. The conductivity of sample NH0 increased by a factor of 2.5 times from 3.5 to $8.9 \times 10^{-5}$ S/m after the generation of pore water but the ECM remains the same (Figure 7).

Conductivity data are typically fit to an Arrhenius expression when they exhibit an exponential temperature dependence, suggesting that the material possesses thermally activated charge carrier transport properties (Bloom & Heymann, 1947; Yoshino et al., 2012). The Arrhenius relation for conductivity as a function of temperature is expressed as

$$\sigma(T) = \sigma_0 e^{-\left(\frac{E_a}{RT}\right)} \tag{1}$$

where $\sigma_0$ is a preexponential constant (S/m), $E_a$ is the activation energy (kJ/mol), $R$ is the gas constant (8.314 J/mol/K), and $T$ is the temperature (K). The preexponential term in equation (1) can be derived as the linear slope in each plot in Figure 7 to get a specific activation energy ($E_a$) (see equations S1–S3 in the supporting information). Activation volume was not carefully measured, but pressures up to ~20 MPa have little effect on electrical conductivity of hydrate bearing samples (Du Frane et al., 2015), and can therefore be assumed to be small. This allows us to effectively determine activation energy from fitting electrical

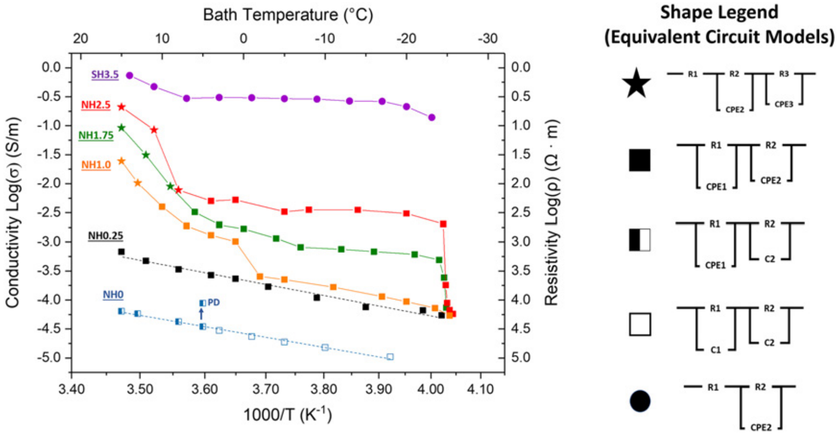

**Figure 7.** Conductivity log plot as a function of temperature for all methane hydrate samples. Each data point is fitted with an equivalent circuit model and markers are shown as different geometric symbols. Point PD shows the partially dissociated methane hydrate sample after generating pore water within it. The conduction pathways appear to change as a function of sample composition and corresponding conductivity values. Pure methane hydrate (NH0) has the lowest conductivity while methane hydrate synthesized from frozen seawater (SH3.5) has the highest conductivity for the entire temperature range measured. Conductivity of hydrate samples with added NaCl (NH0.25–NH2.5) plots in between these two extremes.

conductivity measured on the NH0 and N0.25 samples despite isochoric pressure variations during temperature cycling. Pure methane hydrate (sample NH0) was calculated to have an activation energy of 33.5 kJ/mol, which is similar to other reports at 30.6 kJ/mol (Du Frane et al., 2011). For sample NH0.25 with a minute amount of salt added, the activation energy is still roughly the same as sample NH0 at 36.6 kJ/mol, but is an order of magnitude more conductive. However, for higher salt content samples, temperature and conductivity no longer have a log linear relationship across the full temperature range. Significantly higher activation energies (illustrated by the steeper slopes) are observed at both the higher temperature (>0 °C) and lower temperature (<−24 °C) regions (Figure 7). The sharp changes in the log conductivity behavior implies these samples (or parts of the samples) were undergoing phase changes, which has been previously observed in ice and other materials (Buehler et al., 2007; Presnall et al., 1972).

## 4. Discussion

The electrical properties of methane hydrate mixture systems were found consistent with the general concept that higher total salt content leads to higher electrical conductivity due to the increase of ionic charge carriers. However, grain-scale-level uniformity of salt distribution throughout the samples remains uncertain, as does whether local salinity inhomogeneity might affect electrical properties. NaCl-bearing phases along methane hydrate grain boundaries are shown to be partially interconnected in at least some sections of samples, and grain junctions possessing higher concentrations of NaCl are suggested from SEM and EDS analysis (Figures S2c–S2h). During the initial stages of hydrate formation, the synthesis process will consume some or most $H_2O$ to form methane hydrate, but some $H_2O$ is diverted into dissolving NaCl salt. Upon further melting and freezing cycles, more $H_2O$ is converted to methane hydrate, resulting in progressively higher brine salinity in localized pockets (Chaouachi et al., 2015; Chen & Espinoza, 2018). It is possible that some regions of high salt concentration will migrate to regions of low salt concentration until an equilibrium state is reached where the brine is near or fully saturated, and where no more methane hydrate will be synthesized from the fluid phase. The eventual stabilization (typically after the third cycle) and repeatability of impedance measurements in any one sample suggests that an equilibrium or near-equilibrium is indeed reached in all samples prior to the final step-dwell measurement (Figure 4). However, we cannot rule out that at least some local regions may not be interconnected along hydrate grain boundaries, leading to possible heterogeneous salinity in samples. Chen et al. (2018) were able to prove their samples were inhomogeneous in salinity by using micro-CT to observe the migration of brine (NaBr and KI) and quantitatively measure the salinity changes in different regions during methane hydrate synthesis. Moreover, our own documentation of NaCl-bearing crystalline development in certain regions of samples (e.g., Figures 3c–3e and S2b–S2h) supports

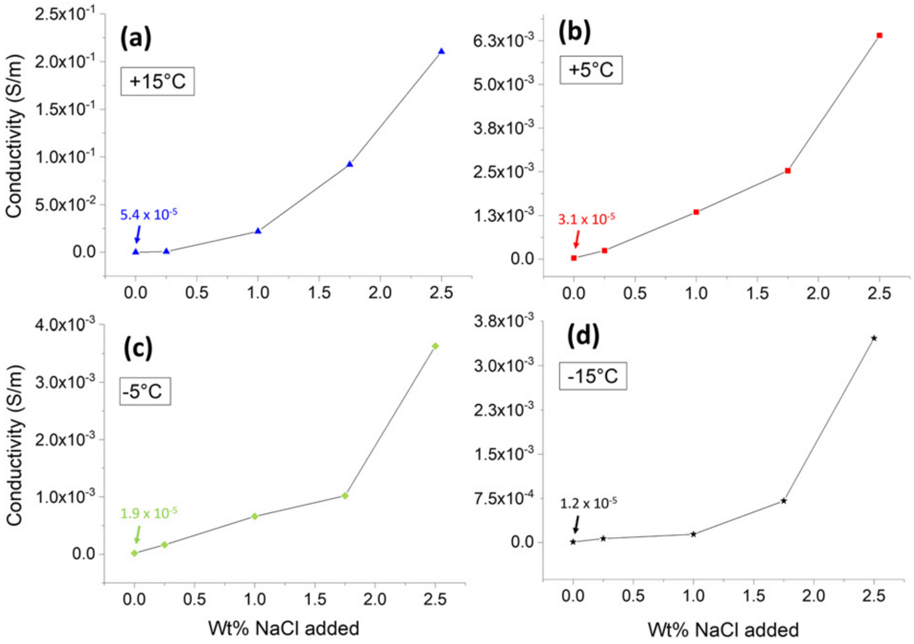

**Figure 8.** Conductivity plot as a function of bulk NaCl content for (a) +15 °C, (b) +5 °C, (c) −5 °C, and (d) −15 °C. An exponential increase in conductivity is observed for methane hydrate samples with NaCl added. +5 °C to −5 °C are relevant temperature conditions of natural hydrate deposits.

this hypothesis. Hence, adding more salt may increase the formation of more brine networks and local brine salinity, resulting in greater increases in conductivity. We observe this effect as exponential increases in conductivity when we compare all "NH" samples at +5 °C and +15 °C (Figures 8a and 8b).

The residual fluid phase is expected to become increasingly concentrated in NaCl as ice starts to crystallize. Since the body of the pressure vessel transmits heating or cooling from the perimeter of the sample inward, the sample may experience a thermal gradient where brine at the center of the sample will melt or freeze last, respectively. Therefore, the center of the sample may have a relatively higher salinity when the sample is cooled below the hydrohalite solidus. This is evident when the heating and cooling rates of the samples are compared. Salt crystal precipitation during cooling is typically a slower process than dissolution by heating. Because of this kinetic difference, we observed hysteresis in all samples except the pure methane hydrate with no salt added (sample NH0; Figure 9). To this end, our reported conductivity values are accurate based on a step-dwell heating method where both thermal and chemical equilibrium were more likely to have been reached.

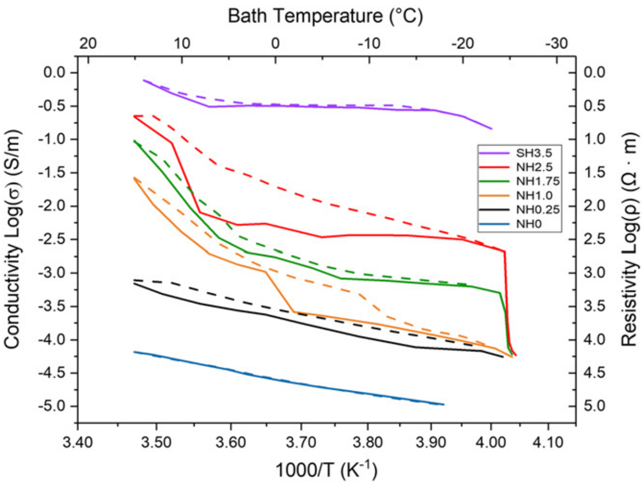

**Figure 9.** Log-conductivity plot of all runs for both step-dwell heating (solid line) and natural freezer cooling (dotted line) measurements. A hysteresis is observed for all samples except pure methane hydrate with no salt added (sample NH0).

Based on molecular modeling studies of gas hydrate, nonpolar guest species such as methane may not possess guest-host hydrogen bonds, nor do they have the same Bjerrum intrinsic defects as ice (Alavi et al., 2009). This may explain the higher resistivity of methane hydrate relative to ice (Du Frane et al., 2011). Like ice, when low levels of salt impurities exist (sample NH0 and NH0.25), the ionic charge carriers (extrinsic defects) are transported by thermally activated solid-state diffusion mechanisms (Barnes & Wolff, 2004; Du Frane et al., 2011; Kulessa, 2007). This is reflected in their log linear conductivity behavior relative to temperature indicating there is no significant phase change affecting conductivity (Figures 7 and 9). While this could suggest that the small NaCl fraction added is simply positioned at the interstitial grain boundaries and not forming enough brine to be well-connected (sample NH0.25), a better explanation that, supported by additional evidence discussed below, may be that the small NaCl fraction is incorporated into the methane hydrate structure itself as an impurity or doping agent. With increasing salt content at the bulk-sample level, a percolation threshold is then crossed (>0.25 wt % NaCl) and sufficient salt ions begin to interact with the dipole of the $H_2O$ molecules in the methane hydrate lattice, destabilizing them, and forming a conductive brine network (Sylva et al., 2016). The existence of an interconnected liquid phase changes the primary pathway for electric current (no longer solely solid-state hopping mechanisms) as observed from the nonlinear log conductivity behavior of samples with higher salt contents (Figures 7 and 9).

At increasing temperatures above the liquidus, conductivity begins to sharply increase for higher salt content samples (NH1.0–SH3.5). One possible explanation involves an increase in pore water that could form from partial dissociation of the methane hydrate phase. Since localized regions of these samples may have saturated levels of brine (23 wt % NaCl), it is possible that the ~19 °C phase stability temperature for pure methane hydrate can drop down to ~13 °C at ~20-MPa conditions (Cha et al., 2016; Jager & Sloan, 2001; Hu et al., 2017). Hence, the higher temperature regions are possibly unstable for localized regions of methane hydrate with high-salinity brine. As observed in the partially dissociated pure methane hydrate sample (NH0), generating pore liquid can cause a substantial increase in conductivity (Figure 2a). Several simple petrophysical two-phase mixing models (Archie's law and other derivatives) also suggest brine melt fractions can potentially reach up to 10 vol % at +15 **°C** for sample NH2.5 (Table S3) (Archie, 1942; Hermance, 1979). Furthermore, the additional pore water generated from hydrate dissociation may dissolve neighboring excess NaCl(s), which could increase the concentration of ionic carriers (increased salinity) in the liquid brine phase that dictates the conductivity of the system (Resistivity of NaCl Water Solutions, 2009).

Between the liquidus and solidus, ice, halite, hydrohalite, and brine can all coexist but in varying proportions depending on temperature and salinity. As temperature approaches the liquidus from below, the brine-to-hydrohalite ratio will increase as more hydrohalite melts incongruently into halite and saturated brine. The amount and/or distribution of hydrohalite may be insufficient, however, to produce enough brine to affect conductivity significantly. This is a possible explanation for the relatively small changes in the log conductivity observed in the temperature regime between the liquidus and solidus (Figure 7).

When the temperature drops to the solidus, the last remaining volume of liquid (brine) will "freeze" into a solid eutectic mixture of ice and hydrohalite (Figures S2g, S2h, and S2i) and causes the log conductivity of all NaCl-bearing samples to drop to roughly the same level (−24 °C in Figure 7). The hydrohalite solidus in a NaCl-H2O system is typically −21 °C, but due to kinetics and sample temperature lag inside the vessel, we do not observe this phenomenon until the bath temperature reaches −24 °C (De Roo et al., 1983; Grimm et al., 2008; Light et al., 2009). At this point, all conduction mechanisms will be purely by hopping of charge carriers in a solid-state mixture composed of ice, hydrohalite, methane hydrate, and any undissolved halite (Figure 1). Similar sharp changes in conductivity have been observed in NaCl-H2O mixtures where brine channels form into coexisting ice + hydrohalite at the eutectic (Grimm et al., 2008). Also, like ice, methane hydrate might not completely exclude salt ions from its crystal lattice, particularly during late-stage synthesis under the closed-system conditions here, and instead low concentrations (~ppm) may be soluble in the lattice, increasing the conductivity of the system (Buehler et al., 2007; Conde et al., 2017; Petrenko & Whitworth, 1999). *Du Frane et al.* were able to model and show that impurities from the sand act as dopants and contribute to the conductivity of methane hydrate mixtures proportional to the volume fraction of the sand added up to 45 vol % sand (Du Frane et al., 2015, section S1 and equation S5). Similarly, it is possible some amount of NaCl can be incorporated into the methane hydrate lattice as charge carriers, regardless of the overall NaCl concentration added. Thus, all hydrate samples with NaCl exhibit similar conductivities below the solidus when there is no liquid brine to obscure the doping effect (−24 °C in Figure 7). Also, since hydrohalite has a lower conductivity ($<10^{-4}$ S/m) than doped methane hydrate ($>10^{-4}$ S/m), the doped methane hydrate becomes the dominant conduction pathway and this may well explain why the minimum conductivity is at the level of sample NH0.25 and not sample NH0 or lower levels (Grimm et al., 2008).

Equivalent circuit models can provide insight into the conditions that cause conduction mechanisms to undergo significant change, which is not always exhibited in the activation energy or the absolute magnitude of the conductivity. In the ECM for samples NH1.0, NH1.75, and NH2.5, the high-temperature regime is determined to have the conduction circuit model "R+RCPE+RCPE." The unpaired third resistor element in series may potentially exist in all NaCl samples but is negligible contributor to the bulk sample resistance. This third resistor element has a small value and becomes resolvable only when the bulk conductivity is high enough ($>10^{-2}$ S/m) or vice versa, bulk resistivity is low enough ($<10^{2}$ Ω/m). If this third resistor element represents brine and is "in series" instead of "in parallel" based on the ECM, this may indicate the brine network is not 100% interconnected between the two silver electrodes, as originally suspected. It is possible that charge carriers need to travel through both a liquid and a solid phase in order to move through the sample. On the other hand, sample SH3.5 with an ECM of "R+RCPE" was prepared via flash-freezing using liquid $N_2$ (Figure 6e). Perhaps this method creates greater salt uniformity at the grain-scale level, which allows a fully interconnected brine network to form. Although the dielectric response of sample SH3.5 is not fully resolved in the frequency range measured, the highly conductive system can still be accurately modeled as a bulk resistor with negligible capacitance. The ECM suggests the only capacitance detected is from polarization at the electrode-sample interface, similar to a Randles cell, "R+RCPE" (Barsoukov & Macdonald, 2005). Therefore, these different spectral behaviors between samples NH2.5 and SH3.5 indicate electrical properties of methane hydrate are strongly dependent not only on salinity, but also salt distributions.

In summary, we see three conduction regimes: (1) at the lowest test temperatures below the solidus or at the lowest salinity, conduction is primarily by solid state diffusion of ionic defects in methane hydrate with no liquid. (2) Between the solidus and liquidus, where a connected saturated brine network forms for higher-salinity samples and coexists with hydrohalite and ice, conduction depends greatly on the brine-hydrohalite ratio but not significantly on temperature. (3) Above the liquidus, upon final melting of ice and hydrohalite, conduction is governed by the salinity (dissolved solute concentration) and volume of the brine network. In natural marine environments, gas hydrate-bearing systems form above the liquidus and hence conductivity will be dominated by pore liquids (brine). Regardless, with the many kinetic factors to consider in these complicated mixed-phase systems, reaching thermodynamic and chemical equilibrium in the laboratory —by controlling time, temperature, and composition—is extremely important for obtaining accurate measurements that are relevant to the full range of conditions where gas hydrates can form in nature.

## 5. Conclusions

We measured the electrical properties of methane hydrate coexisting with brine and excess $CH_4$ gas over a wide range of temperatures, including those relevant to gas hydrate occurrences in nature, and quantified the effect of NaCl on bulk-sample conductivity. Impedance and electrical conductivity for mixtures containing methane hydrate and NaCl-bearing brine were found to be most sensitive to the connectivity, overall concentration of ionic solutes (salinity) and melt fraction that occurs at higher temperatures. The distribution of the fluid phase becomes less important, however, once connected.

The effect of adding NaCl when synthesizing methane hydrate is profound. Adding NaCl influences the crystal habit development, causing highly rounded and irregular morphologies with increasing NaCl concentration. In regard to electrical properties, accumulation of ~$15 \pm 5$ vol % pure $H_2O$ pore water within samples at +5 °C increases conductivity by approximately half a log scale relative to pure methane hydrate, whereas NaCl-brine elicits an *exponential* increase in conductivity with increasing concentrations of solute. At the geologically relevant temperature of +5 °C, the addition of 2.5 wt % NaCl increases conductivity by over 2 orders of magnitude relative to pure methane hydrate. Methane hydrate synthesized from seawater (SH3.5, with 2.7 wt % NaCl and 0.8 wt % as other salts) exhibits even higher conductivities at +5 °C, suggesting that similar effects on conductivity are produced by other ionic compounds as well. At salt concentrations low enough to prevent a well-connected brine phase from forming, the presence of salt still exerts significant influence on electrical conductivity. Adding 0.25 wt % NaCl to the initial ice reactant was found to effectively dope the resulting methane hydrate, and increased conductivity by ~1 order of magnitude compared with pure methane hydrate over the measured temperature range. Furthermore, *all* NaCl-bearing samples tested here are presumed to contain doped methane hydrate upon late-stage synthesis, based on low-temperature (<−24 °C) impedance measurements of all NaCl-bearing samples converging to the doped-hydrate value after final freezing or crystallization of coexisting brine. ECM provided valuable information in combination with phase equilibria and impedance spectroscopy that confirmed brine as the conduction pathway in samples with high salt content and at high temperatures, while cryo-SEM verified the connected nature of the brine and the apparent formation of hydrohalite within it upon cooling to subsolidus temperatures.

These findings highlight what are likely only a few of the effects that salts may impart on the formation and conductivity of methane hydrate in nature. Phase changes within the brine component that accompany each thermal cycling event during sample synthesis here—including repeated formation and eventual melting/dissolution of ice, hydrohalite, and halite—complicate the role of temperature dependence on bulk sample conductivity. The evolution and connectivity of gas-filled pore space during synthesis may result in additional effects, although presumably minimal due to the electrically insulating properties of gas itself at the test conditions here. Nonetheless, we show that conductivity of the bulk samples is predominantly influenced by salinity changes and the presence of pore liquid, and these results can in turn benefit gas hydrate saturation models.

Other characterization techniques such as micro-computed tomography (μCT) can give additional insights into wetting angle behaviors by revealing hydrate pore sizes and fluid volumes. Further coupling of impedance spectroscopy with imaging capabilities of μCT may help in correlating bulk conductivity with the formation of methane hydrate and the evolution of brine channels, as well as changes in localized salinity as a function of temperature and time. These combined techniques, for instance, may enable better understanding of variables that destabilize or limit gas hydrate growth in natural environments containing free-phase methane gas, such as those proximal to gas chimneys where water-limited or salt-limited multiphase environments exist (Liu & Flemings, 2007).

Lastly, we note that our experimental results are obtained under closed-system conditions where salt concentration remains constant at the bulk sample level, but that may reach highly or fully saturated levels in the coexisting brine as hydrate synthesis nears completion. While such high-salinity brines may not necessarily form in more open systems with greater flux of seawater, particularly over geologic time scales, we show that simple petrophysical mixing models such as Archie's law can still help infer pore water fractions even in methane hydrate samples with little-to-no salt impurities (Table S3). Electromagnetic remote sensing studies in the field can also benefit from the salinity-conductivity insights gained from this work to aid interpretation of field data. For instance, while the role of brine might be very different in an open system dominated by seawater than for our closed system measurements, we have shown that the presence of NaCl will increase the electrical conductivity of hydrate by about an order of magnitude over pure methane hydrate, to a conductivity represented by NH0.25. This is similar to the effect observed by Du Frane et al. (2015) associated with impurities derived from natural sand grains, which also increased conductivity by about an order of magnitude. The use of Archie's law for the interpretation of well logs and field CSEM results requires the inclusion of hydrate conductivity for high hydrate saturations, where the role of seawater in the pore space is diminished. Such high concentrations have been observed by Matsumoto et al. (2017), with well logs peaking at about 2,000 Ω/m resistivity ($5 \times 10^{-4}$-S/m conductivity) in fairly good agreement with our measurements for methane hydrate formed in the presence of NaCl. The relationship between the coexisting fluid phase and conductivity is applicable to both closed and open systems as long as salinity, pressure, and temperatures are known. For natural gas-hydrate bearing formations with additional components and/or sediment fractions to account for, more complex mixing models to accurately infer gas hydrate concentration will be required.

**Acknowledgments**
Support for this work was provided by U.S. Department of Energy contract DE-FE0028972 and Interagency Agreement DE-FE0026382 between the USGS Gas Hydrate Project and DOE/NETL. Prepared by LLNL under contract DE-AC52-07NA27344. IM release number: LLNL-JRNL-777845. Any use of trade, firm, or product names is for descriptive purposes only and does not imply endorsement by the U.S. Government. The authors wish to thank P. Kannberg (SIO), W. Waite (USGS), D. Lockner (USGS), A. Cook (OSU), and an anonymous reviewer for the constructive comments on the manuscript. Raw data for this research work are available on the Open Source Framework repository DOI:10.17605/OSF.IO/MJQ6P

## References

Alavi, S., Susilo, R., & Ripmeester, J. A. (2009). Linking microscopic guest properties to macroscopic observables in clathrate hydrates: Guest-host hydrogen bonding. *Journal of Chemical Physics*, *130*(17), 174501. https://doi.org/10.1063/1.3124187

Archer, D. (2007). Methane hydrate stability and anthropogenic climate change. *Biogeosciences*, *4*(4), 521–544. https://doi.org/10.5194/bg-4-521-2007

Archie, G. E. (1942). The electrical resistivity log as an aid in determining some reservoir characteristics. *Transactions of AIME*, *146*, 54–67.

Attias, E., Weitemeyer, K., Holz, S., Naif, S., Minshull, T. A., Best, A. I., et al. (2018). High-resolution resistivity imaging of marine gas hydrate structures by combined inversion of CSEM towed and ocean-bottom receiver data. *Geophysical Journal International*, *214*(3), 1701–1714. https://doi.org/10.1093/gji/ggy227

Attias, E., Weitemeyer, K., Minshull, T. A., Best, A. I., Sinha, M., Jegen-Kulcsar, M., et al. (2016). Controlled-source electromagnetic and seismic delineation of subseafloor fluid flow structures in a gas hydrate province, offshore Norway. *Geophysical Journal International*, *206*(2), 1093–1110. https://doi.org/10.1093/gji/ggw188

Barnes, P. R. F., & Wolff, E. W. (2004). Distribution of soluble impurities in cold glacial ice. *Journal of Glaciology*, *50*(170), 311–324. https://doi.org/10.3189/172756504781829918

Barsoukov, E., & Macdonald, J. R. (2005). Physical and Electrochemical Models. In *Impedance Spectroscopy: Theory, Experiment, and Applications* (2nd ed., chap. 2.2, pp. 80–129). Hoboken, NJ: John Wiley & Sons Inc.

Bloom, H., & Heymann, E. (1947). The electrical conductivity and the activation energy of ionic migration of molten salts and their mixtures. *Proceedings of the Royal Society of London Series A-Mathematical and Physical Sciences*, *188*(1014), 392–414. https://doi.org/10.1098/rspa.1947.0016

Bondarenko, A. S., & Ragoisha, G. A. (2005). In A. L. Pomerantsev (Ed.), *Progress in Chemometrics Research* (pp. 89–102, Version 16.07.2013 (the program is available online at). New York: Nova Science Publishers. http://www.abc.chemistry.bsu.by/vi/analyser/

Boswell, R., & Collett, T. S. (2011). Current perspectives on gas hydrate resources. *Energy & Environmental Science*, *4*(4), 1206–1215. https://doi.org/10.1039/c0ee00203h

Buehler, M. G., Chin, K. B., Seshadri, S., Keymeulen, D., Anderson, R. C., & McCann, T. A. (2007). Electrical properties probe measures water/ice content of martian soils using impedance spectroscopy, paper presented at 2007 IEEE Aerospace Conference, Big Sky, MT, Mar 03-10.

Cai, J., Wei, W., Hu, X., & Wood, D. A. (2017). Electrical conductivity models in saturated porous media: A review. *Earth-Science Reviews*, *171*, 419–433.

Cha, M. J., Hu, Y., & Sum, A. K. (2016). Methane hydrate phase equilibria for systems containing NaCl, KCl, and NH4Cl. *Fluid Phase Equilibria*, *413*, 2–9. https://doi.org/10.1016/j.fluid.2015.08.010

Chaouachi, M., Falenty, A., Sell, K., Enzmann, F., Kersten, M., Haberthur, D., & Kuhs, W. F. (2015). Microstructural evolution of gas hydrates in sedimentary matrices observed with synchrotron X-ray computed tomographic microscopy. *Geochemistry, Geophysics, Geosystems*, *16*, 1711–1722. https://doi.org/10.1002/2015GC005811

Chen, X., Espinoza, N., Tisato, N., & Flemings, P. B. (2018). X-ray micro-CT observation of methane hydrate growth and dissociation in sandy sediments, *Abstract H41K-2231 presented at 2018 Fall Meeting, AGU*, Washington, D.C., 13 Dec.

Chen, X. Y., & Espinoza, D. N. (2018). Ostwald ripening changes the pore habit and spatial variability of clathrate hydrate. *Fuel*, *214*, 614–622. https://doi.org/10.1016/j.fuel.2017.11.065

Chong, Z. R., Yang, S. H. B., Babu, P., Linga, P., & Li, X. S. (2016). Review of natural gas hydrates as an energy resource: Prospects and challenges. *Applied Energy*, *162*, 1633–1652. https://doi.org/10.1016/j.apenergy.2014.12.061

Collett, T., Bahk, J. J., Baker, R., Boswell, R., Divins, D., Frye, M., et al. (2015). Methane Hydrates in Nature-Current Knowledge and Challenges. *Journal of Chemical and Engineering Data*, *60*(2), 319–329. https://doi.org/10.1021/je500604h

Conde, M. M., Rovere, M., & Gallo, P. (2017). Spontaneous NaCl-doped ice at seawater conditions: focus on the mechanisms of ion inclusion. *Physical Chemistry Chemical Physics*, *19*(14), 9566–9574. https://doi.org/10.1039/C7CP00665A

Constable, S., Kannberg, P. K., & Weitemeyer, K. (2016). Vulcan: A deep-towed CSEM receiver. *Geochemistry, Geophysics, Geosystems*, *17*, 1042–1064. https://doi.org/10.1002/2015GC006174

Cook, A. E., & Waite, W. F. (2018). Archie's Saturation Exponent for Natural Gas Hydrate in Coarse-Grained Reservoirs. *Journal of Geophysical Research: Solid Earth*, *123*, 2069–2089. https://doi.org/10.1002/2017JB015138

Das, S., & Bhattacharyya, A. J. (2011). Dielectric Relaxation Spectroscopy for Evaluation of the Influence of Solvent Dynamics on Ion Transport in Succinonitrile-Salt Plastic Crystalline Electrolytes. *Journal of Physical Chemistry B*, *115*, 2148–2154.

De Roo, J. L., Peters, C. J., Lichtenthaler, R. N., & Diepen, G. A. M. (1983). Occurrence of methane hydrate in saturated and unsaturated solutions of sodium-chloride and water in dependence of temperature and pressure. *AICHE Journal*, *29*(4), 651–657. https://doi.org/10.1002/aic.690290420

Du Frane, W. L., Stern, L. A., Constable, S., Weitemeyer, K. A., Smith, M. M., & Roberts, J. J. (2015). Electrical properties of methane hydrate plus sediment mixtures. *Journal of Geophysical Research: Solid Earth*, *120*, 4773–4783. https://doi.org/10.1002/2015JB011940

Du Frane, W. L., Stern, L. A., Weitemeyer, K. A., Constable, S., Pinkston, J. C., & Roberts, J. J. (2011). Electrical properties of polycrystalline methane hydrate. *Geophysical Research Letters*, *38*, L09313. https://doi.org/10.1029/2011GL047243

Grimm, R. E., Stillman, D. E., Dec, S. F., & Bullock, M. A. (2008). Low-frequency electrical properties of polycrystalline saline ice and salt hydrates. *Journal of Physical Chemistry B*, *112*, 15,382–15,390.

Hermance, J. F. (1979). The electrical conductivity of materials containing partial melt: A smiple model for Archie's law. *Geophysical Research Letters*, *6*(7), 613–616.

Hesse, R., & Harrison, W. E. (1981). Gas hydrates (clathrates) causing pore-water freshening and oxygen isotope fractionation in deep-water sedimentary sections of terrigenous continental margins. *Earth and Planetary Science Letters*, *55*, 453–462. https://doi.org/10.1016/0012-821X(81)90172-2

Hornbach, M. J., Holbrook, W. S., Gorman, A. R., Hackwith, K. L., Lizarralde, D., & Pecher, I. (2003). Direct seismic detection of methane hydrate on the Blake Ridge. *Geophysics*, *68*(1), 92–100. https://doi.org/10.1190/1.1543196

Hu, Y., Lee, B. R., & Sum, A. K. (2017). Phase equilibrium data of methane hydrates in mixed brine solutions. *Journal of Natural Gas Science and Engineering*, *46*, 750–755. https://doi.org/10.1016/j.jngse.2017.08.004

Jager, M. D., & Sloan, E. D. (2001). The effect of pressure on methane hydration in pure water and sodium chloride solutions. *Fluid Phase Equilibria*, *185*(1-2), 89–99. https://doi.org/10.1016/s0378-3812(01)00459-9

Kulessa, B. (2007). A critical review of the low-frequency electrical properties of ice sheets and glaciers. *Journal of Environmental and Engineering Geophysics*, *12*(1), 23–36. https://doi.org/10.2113/jeeg12.1.23

Kuustraa, V. A., & Hammershaimb, E. C. (1983). *Handbook of Gas Hydrate Properties and Occurrence* (U.S. Dept of Energy Publication) DOE/MC/19239-1546. Washington, DC: Lewin and Associates, Inc.

Kvenvolden, K. A. (2000). Gas hydrate and humans. *Gas Hydrates: Challenges for the Future*, *912*, 17–22. https://doi.org/10.1111/j.1749-6632.2000.tb06755.x

Lee, J. Y., Santamarina, J. C., & Ruppel, C. (2010). Parametric study of the physical properties of hydrate-bearing sand, silt, and clay sediments: 1. Electromagnetic properties. *Journal of Geophysical Research*, *115*, B11104. https://doi.org/10.1029/2009JB006669

Lee, M. W., & Collett, T. S. (2011). In-situ gas hydrate hydrate saturation estimated from various well logs at the Mount Elbert Gas Hydrate Stratigraphic Test Well, Alaska North Slope. *Marine and Petroleum Geology*, *28*(2), 439–449. https://doi.org/10.1016/j.marpetgeo.2009.06.007

Li, F. G., Sun, C. Y., Li, S. L., Chen, G. J., Guo, X. Q., Yang, L. Y., et al. (2012). Experimental Studies on the Evolvement of Electrical Resistivity during Methane Hydrate Formation in Sediments. *Energy & Fuels*, *26*(10), 6210–6217. https://doi.org/10.1021/ef301257z

Liang, J. Q., Zhang, Z. J., Su, P. B., Sha, Z. B., & Yang, S. X. (2017). Evaluation of gas hydrate-bearing sediments below the conventional bottom-simulating reflection on the northern slope of the South China Sea. *Interpretation-a Journal of Subsurface Characterization*, *5*(3), SM61–SM74. https://doi.org/10.1190/int-2016-0219.1

Light, B., Brandt, R. E., & Warren, S. G. (2009). Hydrohalite in cold sea ice: Laboratory observations of single crystals, surface accumulations, and migration rates under a temperature gradient with application to Snowball earth. *Journal of Geophysical Research*, *114*, C07018. https://doi.org/10.1029/2008JC005211

Liu, X., & Flemings, P. B. (2007). Dynamic multiphase flow model of hydrate formation in marine sediments. *Journal of Geophysical Research*, *112*, B03101. https://doi.org/10.1029/2005JB004227

Lu, R., Stern, L. A., Du Frane, W. L., Pinkston, J. C., & Constable, S. (2018). Electrical Conductivity of Methane Hydrate with Pore Fluids: New Results from the Lab. *Fire in the Ice*, *18*, 7–11.

Majumdar, U., Cook, A. E., Shedd, W., & Frye, M. (2016). The connection between natural gas hydrate and bottom-simulating reflectors. *Geophysical Research Letters*, *43*, 7044–7051. https://doi.org/10.1002/2016GL069443

Maslin, M., Owen, M., Betts, R., Day, S., Dunkley Jones, T., & Ridgwell, A. (2010). Gas hydrates: past and future geohazard? *Philosophical Transactions of the Royal Society A-Mathematical Physical and Engineering Sciences*, *368*(1919), 2369–2393. https://doi.org/10.1098/rsta.2010.0065

Matsumoto, R., Tanahashi, M., Kakuwa, Y., Snyder, G. L., Ohkawa, S., Tomaru, H., & Morita, S. (2017). Recovery of thick deposits of massive gas hydrates from gas chimney structures, eastern margin of Japan Sea: Japan Sea Shallow Gas Hydrate Project. *Fire in the Ice*, *17*(1), 1–6.

McCarthy, C., Cooper, R. F., Kirby, S. H., Rieck, K. D., & Stern, L. A. (2007). Solidification and microstructures of binary ice-I/hydrate eutectic aggregates. *American Mineralogist*, *92*, 1550–1560.

McIver, R. D. (1981). Gas hydrates. In R. F. M. J. C. Olson (Ed.), *Long-term energy resources* (pp. 713–726). Boston: Pitman.

Petrenko, V. F., & Whitworth, R. W. (1999). *Physics of Ice*. Oxford: Oxford University Press.

Presnall, D. C., Simmons, C. L., & Porath, H. (1972). Changes in electrical conductivity of a synthetic basalt during melting. *Journal of Geophysical Research*, *77*(29), 5665–5672. https://doi.org/10.1029/JB077i029p05665

Ren, S. R., Liu, Y. J., Liu, Y. X., & Zhang, W. D. (2010). Acoustic velocity and electrical resistance of hydrate bearing sediments. *Journal of Petroleum Science and Engineering*, *70*(1-2), 52–56. https://doi.org/10.1016/j.petrol.2009.09.001

Resistivity of NaCl Water Solutions (2009). Schlumberger Log Interpretation Charts 2009 edition, page 8. http://pages.geo.wvu.edu/~tcarr/pttc/schlumberger_chartbook.pdf

Roberts, J. J. (2002). Electrical properties of microporous rock as a function of saturation and temperature. *Journal of Applied Physics*, *91*(3), 1687–1694. https://doi.org/10.1063/1.1430544

Roberts, J. J., & Tyburczy, J. A. (1994). Frequency-dependent electrical properties of minerals and partial melts. *Surveys in Geophysics*, *15*(2), 239–262. https://doi.org/10.1007/bf00689861

Roberts, J. J., & Tyburczy, J. A. (1999). Partial-melt electrical conductivity: Influence of melt composition. *Journal of Geophysical Research*, *104*(B4), 7055–7065. https://doi.org/10.1029/1998JB900111

Rodriquez Presa, M. J., Tucceri, R. I., Florit, M. I., & Posadas, D. (2001). Constant phase element behavior in the poly(o-toluidine) impedance response. *Journal of Electroanalytical Chemistry*, *502*(1-2), 82–90.

Ruppel, C. D. (2015). Permafrost-Associated gas hydrate: Is it really approximately 1% of the global system? *Journal of Chemical and Engineering Data*, *2015*(60), 429–436. https://doi.org/10.1021/je500770m

Ruppel, C. D., & Kessler, J. D. (2017). The interaction of climate change and methane hydrates. *Reviews of Geophysics*, *55*, 126–168. https://doi.org/10.1002/2016RG000534

Shedd, W., Boswell, R., Frye, M., Godfriaux, P., & Kramer, K. (2012). Occurrence and nature of “bottom simulating reflectors” in the northern Gulf of Mexico. *Marine and Petroleum Geology*, *34*, 31–40.

Shoar Abouzari, M. R., Berkemeier, F., Schmitz, G., & Wilmer, D. (2009). On the physical interpretation of constant phase elements. *Solid State Ionics*, *180*(14-16), 922–927. https://doi.org/10.1016/j.ssi.2009.04.002

Sloan, E. D. (1998). Gas hydrates: Review of physical/chemical properties. *Energy & Fuels*, *12*(2), 191–196. https://doi.org/10.1021/ef970164+

Sloan, E. D., & Koh, C. A. (2007). *Clathrate Hydrates of Natural Gases* (3rd ed., Vol. 119, pp. 1–701). Boca Raton, FL: Taylor & Francis Group.

Spangenberg, E., & Kulenkampff, J. (2006). Influence of methane hydrate content on electrical sediment properties. *Geophysical Research Letters*, *33*, L24315. https://doi.org/10.1029/2006GL028188

Stern, L. A., Kirby, S. H., Circone, S., & Durham, W. B. (2004). Scanning electron microscopy investigations of laboratory-grown gas clathrate hydrates formed from melting ice, and comparison to natural hydrates. *American Mineralogist*, *89*(8-9), 1162–1175.

Stern, L. A., Kirby, S. H., & Durham, W. B. (1996). Peculiarities of methane clathrate hydrate formation and solid-state deformation, including possible superheating of water ice. *Science*, *273*(5283), 1843–1848. https://doi.org/10.1126/science.273.5283.1843

Sylva, T. Y., Kinoshita, C. K., & Masutani, S. M. (2016). Inhibiting effects of transition metal salts on methane hydrate stability. *Chemical Engineering Science*, *155*, 10–15.

Trehu, A. M., Long, P. E., Torres, M. E., Bohrmann, G., Rack, F. R., Collett, T. S., et al. (2004). Three-dimensional distribution of gas hydrate beneath southern Hydrate Ridge: constraints from ODP Leg 204. *Earth and Planetary Science Letters*, *222*(3-4), 845–862. https://doi.org/10.1016/j.epsl.2004.03.035

Weitemeyer, K. A., Constable, S., & Trehu, A. M. (2011). A marine electromagnetic survey to detect gas hydrate at Hydrate Ridge, Oregon. *Geophysical Journal International*, *187*(1), 45–62. https://doi.org/10.1111/j.1365-246X.2011.05105.x

Weitemeyer, K. A., Constable, S. C., Key, K. W., & Behrens, J. P. (2006). First results from a marine controlled-source electromagnetic survey to detect gas hydrates offshore Oregon. *Geophysical Research Letters*, *33*, L03304. https://doi.org/10.1029/2005GL024896

Wood, W. T., Gettrust, J. F., Chapman, N. R., Spence, G. D., & Hyndman, R. D. (2002). Decreased stability of methane hydrates in marine sediments owing to phase-boundary roughness. *Nature*, *420*(6916), 656–660. https://doi.org/10.1038/nature01263

Yoshino, T., Shimojuku, A., Shan, S., Guo, X. Z., Yamazaki, D., Ito, E., et al. (2012). Effect of temperature, pressure and iron content on the electrical conductivity of olivine and its high-pressure polymorphs. *Journal of Geophysical Research*, *117*, B08205. https://doi.org/10.1029/2011JB008774

You, K. H., Kneafsey, T. J., Flemings, P. B., Polito, P., & Bryant, S. L. (2015). Salinity-buffered methane hydrate formation and dissociation in gas-rich systems. *Journal of Geophysical Research: Solid Earth*, *120*, 643–661. https://doi.org/10.1002/2014JB011190